PAPER • OPEN ACCESS

Low voltage drop AlGaN UV-A laser structures with transparent tunnel junctions and optimized quantum wells

View the article online for updates and enhancements.

Low voltage drop AlGaN UV-A laser structures with transparent tunnel junctions and optimized quantum wells

Arnob Ghosh[1]**, Agnes Maneesha Dominic Merwin Xavier**[1]**, Syed M N Hasan**[2]**, Sheikh Ifatur Rahman**[1]**, Alex Blackston**[3]**, Andrew Allerman**[4]**, Roberto C Myers**[1,3]**, Siddharth Rajan**[1,3] **and Shamsul Arafin**[1,*]

[1] Department of Electrical and Computer Engineering, The Ohio State University, Columbus, OH 43210, United States of America
[2] National Renewable Energy Laboratory, Golden, CO 80401, United States of America
[3] Department of Materials Science and Engineering, The Ohio State University, Columbus, OH 43210, United States of America
[4] Sandia National Laboratories, Albuquerque, NM 87185, United States of America

E-mail: arafin.1@osu.edu

Abstract

This paper presents the design, material growth and fabrication of AlGaN laser structures grown by plasma-assisted molecular beam epitaxy. Considering hole transport to be the major challenge, our ultraviolet-A diode laser structures have a compositionally graded transparent tunnel junction, resulting in superior hole injection and a low contact resistance. By optimizing active region thickness, a five-fold improvement in photoluminescence intensity is obtained compared to that of our own non-optimized test structures. The electrical and optical characteristics of processed devices demonstrate only spontaneous emission with a peak wavelength at 354 nm. The devices operate up to a continuous-wave current density of 11.1 kA cm^{-2} at room temperature, which is the highest reported for laser structures grown on AlGaN templates. Additionally, they exhibit a record-low voltage drop of 8.5 V to achieve this current density.

Keywords: tunnel junction, UV-A laser, PAMBE, quantum wells, AlGaN

1. Introduction

The development of semiconductor diode lasers emitting ultraviolet (UV) light has generated significant interest due to their various potential applications including air and water purification, disinfection, sterilization, bio-chemical analysis, fluorescence spectroscopy, and high-resolution laser lithography [1, 2]. Specifically, UV-A radiation (320–400 nm) has important applications in the curation of inks, paints, coatings, resins, polymers, and adhesives, as well as three-dimensional (3D) printing for rapid prototyping and light-weight construction [3]. UV light emitting diodes have recently seen improvements in energy efficiency and output power, enabling their use in some of the above-mentioned applications. Unlike these devices, lasers are not fundamentally challenged by the light extraction and efficiency-droop issues, making them suitable for applications that demand high-power/brightness, and spectral purity.

---

* Author to whom any correspondence should be addressed.

J. Phys. D: Appl. Phys. **57** (2024) 035105

A Ghosh *et al*

Electrically pumped (EP) lasers at UV wavelength currently encounter difficulties in achieving continuous wave (CW) operation because of two main challenges. Firstly, the threshold current of nitride lasers are influenced by the design of quantum well (QW)-based gain medium due to the presence of the quantum confined Stark effect (QCSE) [4–6]. It has been observed that in both AlGaN and InGaN-based lasers, threshold current density is highly dependent on the QW width due to QCSE induced by strong spontaneous and piezoelectric polarizations [7–10]. Thus, it is imperative to reduce the QCSE by optimizing the QW width in order to achieve low-threshold UV lasers. Secondly, the *p*-doped cladding layers of AlGaN UV laser structures present challenges due to poor hole injection. The acceptor ionization energy of AlGaN is exceptionally high, and it increases with increasing Al content, leading to limited hole injection from the *p*-AlGaN cladding layer. Higher doping in the *p*-type cladding layer can alleviate the issue, however, the presence of an absorption tail in this heavily doped cladding layer leads to increased optical loss, and threshold current [11, 12]. Additionally, the high effective masses of holes contribute to the high resistivity of *p*-AlGaN layers [13]. Besides, UV-A diode lasers face a significant challenge in creating low-resistance ohmic contacts due to the high mismatch of work functions with metal contacts. To mitigate this challenge, a common approach is the inclusion of a *p*-GaN contact layer. However, *p*-GaN is not transparent to UV light, causing substantial optical absorption loss, which also increases the threshold current.

To overcome all these drawbacks, laser structures with compositionally graded transparent tunnel junctions (TJs) along with an optimized QW active region show promise. The implementation of such TJs in a laser structure allows for the replacement of the resistive *p*-type contact and *p*-AlGaN cladding layer with *n*-AlGaN cladding layers on both the *p*- and *n*-side of the laser structure [14, 15]. As *n*-AlGaN cladding layers have lower activation energy for dopants compared to *p*-AlGaN layer and can form low-resistance ohmic contacts with better current spreading, this laser structure provides improved electrical properties while maintaining low optical losses [16]. While GaN-based transparent TJs with low resistance have been extensively studied [17–20], reports on AlGaN-based transparent TJs are relatively few. Previous work on AlGaN TJs using InGaN [21–25] and GaN [26, 27] as interlayers have shown a very low voltage drop, but these low bandgap interlayers absorb light in UV wavelength, increasing the optical loss. To bypass the optical loss and reduce the threshold current in TJ-based AlGaN lasers with absorbing interlayer, UV transparent homojunction TJs can be implemented. However, AlGaN homojunction TJs show significantly higher voltage losses due to higher tunneling barrier associated with the increased bandgap of AlGaN [28, 29]. Low-resistance transparent TJs through a combination of compositional grading and high doping at the TJ layers have already been reported [30]. We employed the similar approach in our lasers to achieve a low voltage drop and low resistance.

Multiple research groups made significant strides in the development of AlGaN-based lasers. Recently, room temperature (RT) CW lasing with wavelength less than 275 nm was achieved utilizing single crystal AlN substrates [31]. Furthermore, CW-operating lasers with wavelengths of 369 nm [32] and 366 nm [33] were also achieved on bulk GaN substrates. However, realization of CW operation from UV-lasers in the wavelength range between 310 nm and 360 nm, also known as the 'UV-B/A gap' [34], is challenging due to the high lattice mismatch between active layers and high-quality bulk substrates. In this range, lasers emitting at 350.9 nm [35], 353 nm [36], 355 nm [37], 342 nm [38], and 336 nm [39] were fabricated on AlGaN templates that operated only under pulsed conditions. To the best of our knowledge, no EP lasers with CW operation have been reported in this wavelength range.

In this study, we present plasma-assisted molecular beam epitaxy (PAMBE)-grown AlGaN UV-A laser structures with a compositionally graded TJ designed to enhance current injection under CW conditions. We optimized its active region by modifying the AlGaN/GaN QW thickness based on photoluminescence (PL) studies. The growth and material-level characterization of the designed laser materials were also performed. To evaluate the electrical and optical properties of the as-grown material, we fabricated prototype narrow ridge EP lasers emitting spontaneously at 354 nm, which operate up to a CW current density of 11.1 kA cm^{-2} at RT with a record-low forward voltage drop of 8.5 V.

2. Active region optimization

For optimizing the thickness of QWs, PL study was conducted on structures with a single GaN QW and Al$_{0.2}$Ga$_{0.8}$N barriers as shown in figure 1(a). Metal-organic chemical vapor deposition (MOCVD)-grown Al$_{0.3}$Ga$_{0.7}$N templates on sapphire substrates were used for the PAMBE growth. The threading dislocation density (TDD) in the AlGaN templates is about 4×10^9 cm^{-2}. PL samples were grown using Veeco's Gen 930 N$_2$ PAMBE with standard effusion cells of Ga, Mg, Al, and Si. The growth was performed under metal-rich condition at a radio frequency power of 300 W and N$_2$ flow rate of 2 sccm corresponding to a growth rate of 204 nm h^{-1}. Three samples, with varying QW thicknesses of 2.4 nm, 3.4 nm, 4.8 nm while keeping Al$_{0.2}$Ga$_{0.8}$N barriers thickness constant at 8 nm were grown. The RT PL was then measured using a 248 nm NeCu pulsed laser operated at a frequency of 5 Hz and a pulse width of 50 μs with a laser beam spot size of 35 μm. The spectrum was measured using a 110 mm Czerny–Turner monochromator with a grating of 1200 grooves mm^{-1} and a PMT detector.

The RT-PL spectra of the three samples are shown in figure 1(b). The dominant peak at 355 nm is observed from the sample with 2.4 nm thick QW. From a 6-band *k.p* simulation the calculated photon wavelength based on $E_{e1} - E_{hh1}$ transition was predicted to be 355.8 nm and the PL result is
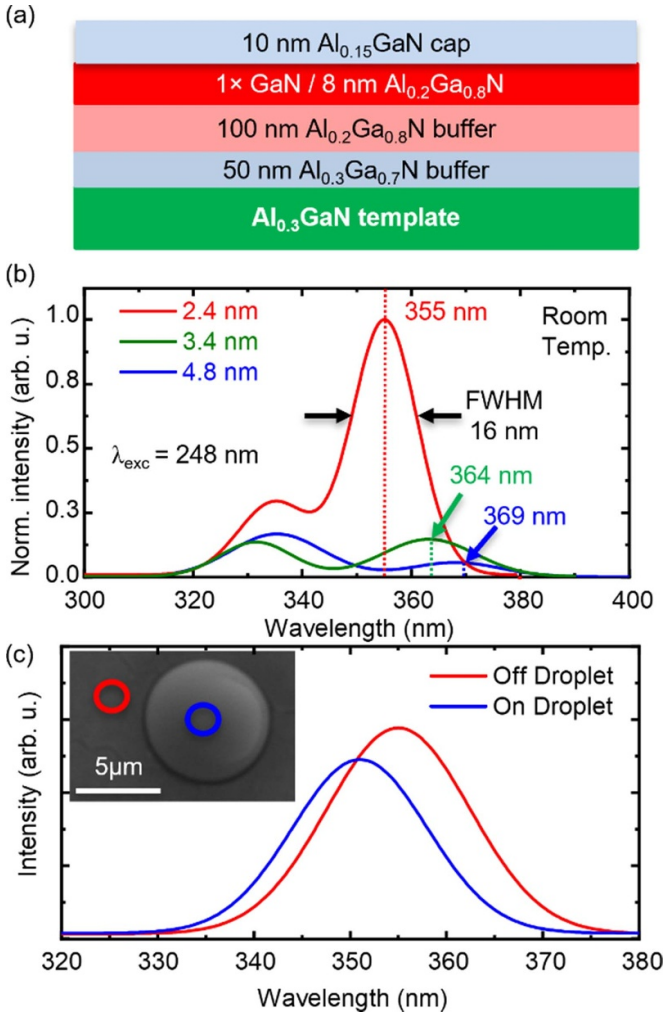
Figure 1. (a) Schematic of the PL structure for photoluminescence study, (b) RT-PL spectra of the three PL samples, and (c) spatial position dependent cathodoluminescent spectra of the PL sample, indicating a blue shift of emission in the on-droplet position compared to off-droplet with an SEM image of the droplet in inset.

in excellent match with the simulated results, indicating this peak originates from $E_{e1} - E_{hh1}$ transition of the QW. The PL full width half maximum (FWHM) of this sample was found to be 16 nm which is higher compared to the other reported active regions of similar wavelength, processed on AlGaN templates with a low dislocation density [38–40]. The large PL FWHM can possibly be attributed to the inhomogeneities caused by the formation of gallium droplets during the growth. As the growth was done under metal rich conditions without any interruption, gallium droplets were formed which are also correlated with dislocation densities. The active region underneath the droplets induces an increase in aluminum composition of the barriers and reduction in QW thickness, yielding a blue shift [41]. The region with the droplet (blue circle) shows a blue shift in PL with respect to the off-droplet (red circle) region, as confirmed by the cathodoluminescent (CL) spectra measured in the sample with 2.4 nm QW as shown in figure 1(c).

For samples with QW width of 3.4 nm and 4.8 nm peak wavelengths shift to 364 nm and 369 nm, respectively. The FWHM of these samples are found to be larger than the one with 2.4 nm QW. The strain of GaN/AlGaN QW in this structure is compressive in nature, which gives rise to large polarization fields and QCSE and thus reduces the overlap between electron and hole wave function. With increased QW thickness, the electron-hole separation further increases. This separation along with quantum size effect reduces the emission energy even below the bulk bandgap and increases the FWHM of the emission spectrum. As a result, material gain will also decrease with increasing thickness resulting in increased threshold current [8, 42].

Considering the simulation results and PL intensity, the sample with 2.4 nm QW performs best and is used in our EP laser structures. It should be noted that the second PL peak at 335 nm in all the three samples corresponds to the emission due to the $Al_{0.15}Ga_{0.85}N$ cap layer.

3. TJ design

A polarization-engineered graded homojunction TJ was utilized in our EP laser structures to achieve efficient hole injection through interband tunneling. In fact, the introduction of the linear compositional grading reduces the tunneling barrier increasing the hole injection efficiency to the active region. The band diagram of the TJ used in the laser structure was simulated using Silvaco Atlas TCAD as shown in figure 2(a). Due to the compositional grading, 3D polarization charges are formed in the *n*- and *p*-doped $Al_xGa_{1-x}N$ of the TJ region, which is superimposed in figure 2(a). The resulting 3D electron and hole gases induce large concentrations of free carriers over the TJ region which pushes the Fermi level closer to the band edge thus reducing depletion related tunneling barriers. It also improves the tunneling probability at a smaller bias voltage, enhancing the carrier tunneling process and contributes to the tunneling current, which was also demonstrated previously [30]. Thus, the graded homojunction TJs result in increased hole concentration and a lower voltage drop compared to non-graded ones and such structure also has the lowest reported voltage penalty [30].

Considering that TJs within the forward-biased devices operate in a reverse direction, the current density–voltage (*J*–*V*) characteristics of the TJ under reverse bias was calculated and illustrated in figure 2(b). The inset showcases the non-local band-to-band tunneling rate of the heavily *n*- and *p*-doped materials.

4. Optical cavity design

A laser cavity was designed using 2D transverse optical mode simulation using complex reflective indices for the emission wavelength of 355 nm. The refractive indices of AlGaN and its alloys were taken from [43] using interpolation. The 1D
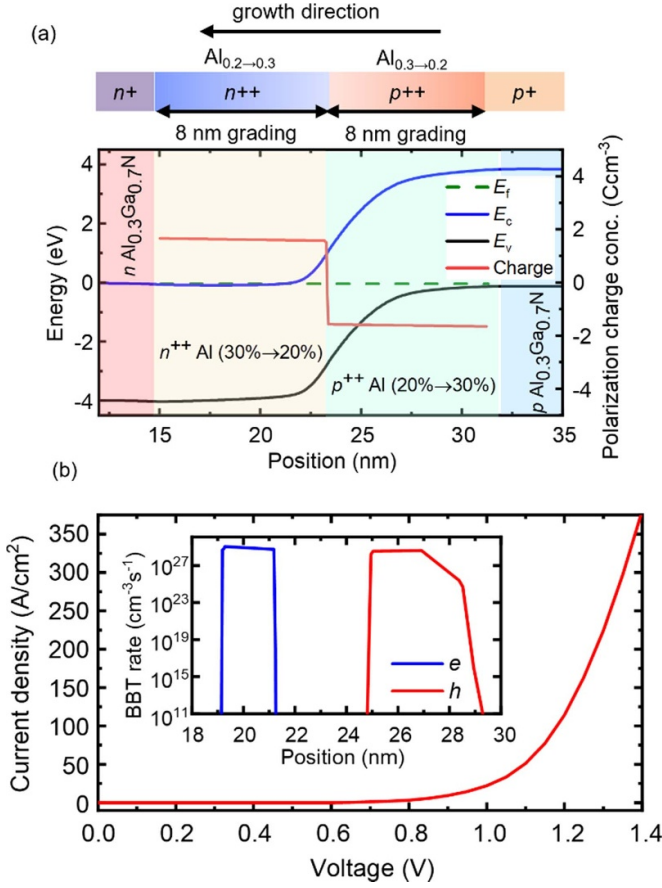
Figure 2. (a) Energy band diagrams of the graded homojunction tunnel junction structure at equilibrium condition with the polarization charge concentration at the interface overlayed on the band diagram indicating 3D charge distribution due to grading of the AlGaN layer reducing the depletion related tunneling barrier, and (b) simulated current density–voltage characteristic of the tunnel junction with the non-local band to band tunneling rate in the inset.

optical intensity of the fundamental transverse electric (TE) mode and the corresponding reflective index profile is illustrated in figure 3(a). The 2D spatial mode distribution of fundamental TE mode is shown in figure 3(b). Although previously it was suggested that an asymmetric waveguide [14–16] is optimum for reducing optical absorption loss in a laser structure with a heterojunction TJ having an absorbing interlayer, in this design, we opted for a symmetric waveguide structure. This choice was made because our homojunction TJ is transparent and will not absorb the light generated by the active region. The thickness of the epitaxial layers was optimized to maximize the overlap of the optical mode with the QW, ensuring a high confinement factor Γ. Simultaneously, careful consideration was given to the composition and lattice constants of the different layers to prevent relaxation of the materials during growth, as they are not lattice-matched to the substrate material. The confinement factor Γ of several regions of the laser is calculated is listed in table 1.
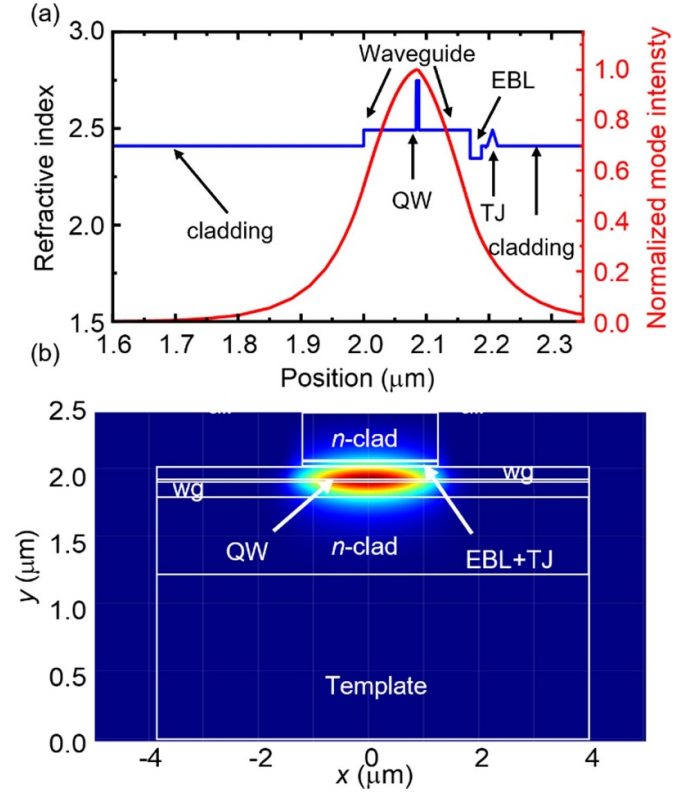

Figure 3. (a) 1D intensity distribution of the mode and refractive index profile in the transverse direction, where effective refractive index $n_{\text{eff}} = 2.45$ is of the fundamental TE mode, and (b) 2D spatial profile of fundamental TE mode.

Table 1. Calculated Γ values for several sections of the laser.

Optical mode in	Confinement factor Γ (%)
Undoped QW	2.0
Top and bottom cladding	25.7
Waveguide layer	67.7
EBL and TJ	4.5
Top contact layer	0.0057

5. Laser material growth and characterization

The epitaxial structure for our PAMBE-grown EP UV-A lasers is shown in figure 4. The growth was initiated with a 300 nm thick n-$Al_{0.3}Ga_{0.7}N$ cladding layer (5×10^{18} cm^{-3} Si doping) at 790 °C. Following the growth of n-cladding layer, 60 nm thick unintentionally doped $Al_{0.2}Ga_{0.8}N$ n-side waveguide layers were grown on both sides of the active region, which consisted of a 2.4 nm GaN singe QW. A 10 nm p-doped $Al_{0.4}Ga_{0.6}N$ layer was used as an electron blocking layer (EBL). A homojunction TJ was then grown on top of this EBL with highly doped p^{++} layer (1×10^{20} cm^{-3} Mg doping) graded down from $Al_{0.3 \to 0.2}Ga_{0.7 \to 0.8}N$ and then a highly doped n^{++} layer (3×10^{20} cm^{-3} Si doping) graded up to $Al_{0.2 \to 0.3}Ga_{0.8 \to 0.7}N$
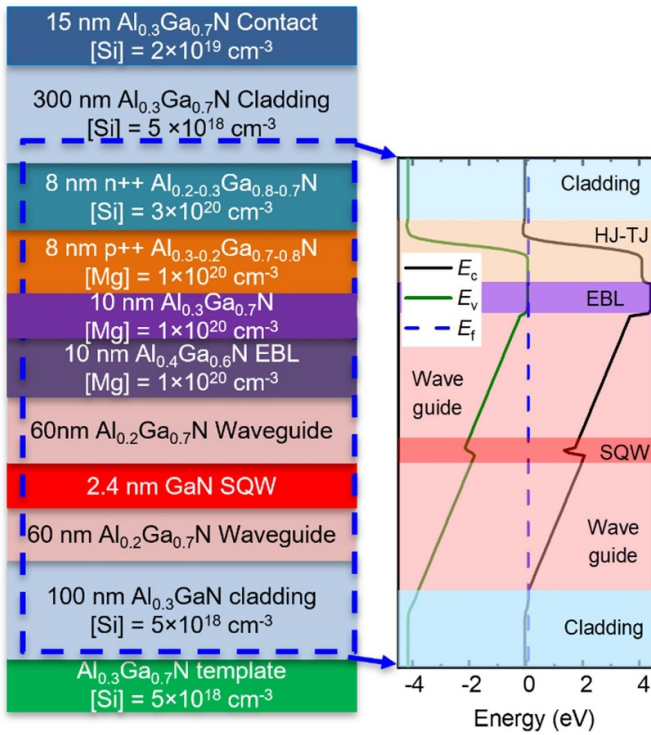
Figure 4. 2D Schematic of UV-A AlGaN laser structures with a transparent HJ-TJ and optimized QWs for the emission wavelength of 355 nm and the band diagram of the structure on the right.

Figure 5. (a) XRD 2θ-ω scan of (002) $Al_xGa_{(1-x)}N$ film, the sharp peak at $34.9°$ and $36°$ correspond to peaks from the template with $x = 30\%$ and 80%, the solder peaks left to the template corresponds to the waveguide and cladding layer, (b) x-ray reciprocal space mapping indicating the cladding and waveguide layers are strained to the template, and (c) 5 μm $\times$ 5 μm AFM image showing the surface morphology of the laser structure.

to take advantage of the induced 3D polarization charge. On top of the TJ, 300 nm $Al_{0.3}Ga_{0.7}N$ *n*-dopped cladding was grown.

After the growth, the crystalline quality and composition of different layers were characterized by high-resolution x-ray diffraction (Bruker D8 Discover). The surface roughness of the as-grown laser structure was examined using AFM (Bruker AXS Dimension Icon). The interface quality and chemical compositions of the layers were investigated by high-angle annular dark-field scanning transmission electron-microscopy (HAADF-STEM) on a JEOL 3100R05 double-corrected STEM operated at 300 kV with energy-dispersive x-ray spectroscopy (EDS). The CL imaging and spectra were measured by a Horiba H-Clue CL system with an iHR320 spectrometer, and 200–900 nm Synapse CCD integrated with a Thermo Scientific Quattro environmental scanning electron microscope. The accelerating voltage for CL observation was 10 kV for optimal CL intensity and spatial resolution.

The high resolution XRD 2θ-ω scan for (002) $Al_xGa_{1-x}N$ film is shown in figure 5(a). The sharp and high intensity peaks at $34.9°$ and $36°$ correspond to $Al_{0.3}Ga_{0.7}N$ and $Al_{0.8}Ga_{0.2}N$ layers of the MOCVD grown template. The PAMBE grown cladding and waveguide layers are also seen as shoulder peaks on the left side of the $Al_{0.3}Ga_{0.7}N$ substrate peak revealing the Al composition of 29% and 22% respectively. X-ray reciprocal space mapping data shown in figure 5(b) perceived that the waveguide layer and the cladding layers are strained to the
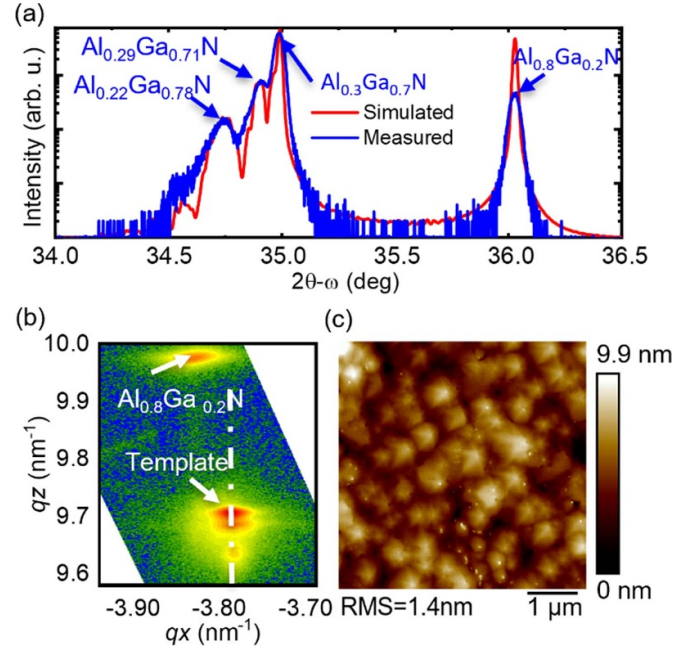
$Al_{0.3}Ga_{0.7}N$ template and were not relaxed. The AFM image of a 5 μm $\times$ 5 μm scan area shown in figure 5(c) reveals clear atomic steps, suggesting the growth was done under metal rich conditions [44]. The surface roughness value of 1.4 nm was obtained.

Figure 6 displays the HAADF-STEM image of our laser structure, revealing several distinct heterointerfaces between the cladding, waveguide, QW, EBL and the TJ. The composition of the waveguide layer found from the energy-dispersive EDS was found to be 22.8% and the bottom cladding to be 29% which matches closely with the compositions extracted from XRD. The interface between the bottom cladding and waveguide layer can be seen clearly by the intensity difference in figure 6(a). The high-magnification image of the red marked region is shown in figure 6(c) which depicts the high crystalline quality and sharp interface of the AlGaN/GaN barriers. Figure 6(b) shows the demagnified image of the top portion of the laser stack. The uniform interface between the EBL and the top waveguide can also be seen due to the intensity variation. However the homojunction TJ region is clearly non-uniform, indicating 3D growth in that region, which might be attributed to high Mg doping. During this 3D growth, some defects were formed which propagated through the top cladding layer as shown by the yellow rectangle. The high-magnification image of a portion the TJ marked by the blue box is shown in figure 6(d) which shows the compositional variation of Al.
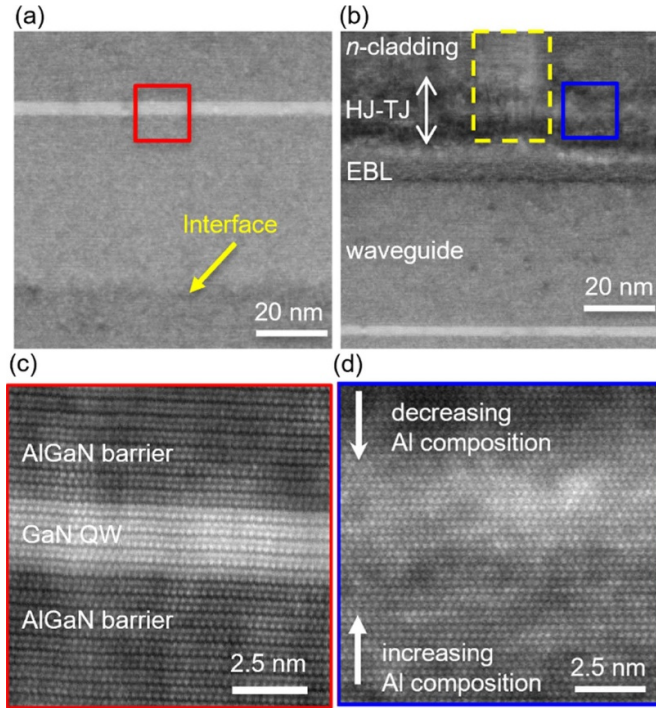
Figure 6. HAADF-STEM image of cross-sectional GaN and AlGaN multilayers consistent with the device design. The low magnification image shows the interfaces between (a) QW, bottom waveguide and the cladding, and (b) the top cladding, waveguide, EBL and homojunction TJs. Some defects are generated in the TJ and propagate through the cladding shown by yellow dotted region. High-resolution images of the (c) AlGaN/GaN/AlGaN QWs/barriers, and (d) the TJ region, corresponding to the red- and blue-marked regions in figure (a) and (b), respectively.

Figure 7. (a) Schematic and optical microscope image of the fabricated device, (b) STEM image of the device cross section.

6. Device fabrication and characterization

After material characterization, prototype lasers as shown in figure 7(a) were fabricated. Narrow ridges of 3 μm were first defined by dry etching the top cladding layer. To form bottom *n*-side contacts, dry etching was done to reach the *n*-doped template. Both the ridge formation and bottom contact opening was done using inductive coupled plasma and reactive ion etching with BCl$_3$, Cl$_2$ and Ar gas plasma. Ti (20 nm)/Al (120 nm)/Ni (30 nm)/Au (50 nm) contact was evaporated for both top *p*-side and bottom *n*-side contacts. The metal contacts were then annealed at 850 °C in N$_2$ ambient condition. The sidewalls were passivated with ALD deposited Al$_2$O$_3$ followed by Ni/Au contact pad deposition. Facets for a 500 μm long laser cavity were formed by a combination of dry and wet etch. The cross-section STEM image of the processed devices is shown in figure 7(b).

The *J*–*V* of these devices were then measured at RT. Figure 8(a) shows the CW *J*–*V* characteristics of the devices. The current density is calculated by dividing the current value by the ridge area (3 μm × 500 μm). The maximum current density obtained from the device is 11.1 kA cm^{-2} which is the highest reported CW current density for laser struct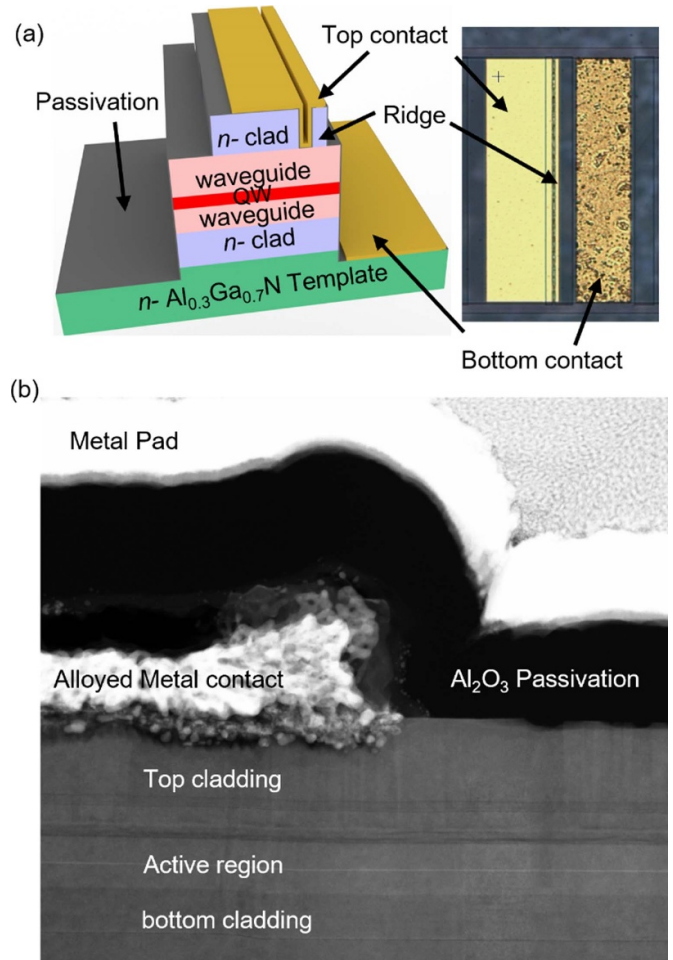ures grown on AlGaN templates at RT. This current density is obtained at just 8.5 V which is drastically lower than other demonstration of UV-A lasers on AlGaN templates using *p*-AlGaN cladding layers [37–40].

Measurements performed on the top *p*-side contact using the transfer length method provides a sheet resistance of 187 $\Omega/\square$ and a contact resistivity of 3.55×10^{-5} Ω cm^2, yielding a low *p*-contact resistance. The differential resistivity of this device is extracted from the slope of the measured current voltage relation followed by subtracting the contact resistances and is shown in the inset of figure 8(a). The value of differential resistivity is in the range of 1–2 × 10^{-4} Ω cm^2 which is lower than *p*-AlGaN counterparts, indicating decent tunneling of carrier [33, 37–40].

The output power obtained from one of the facets is plotted against the current density, as shown in figure 8(b). The output power exhibits an increasing trend with the higher current density, without any significant drop in the slope, suggesting better hole transport compared to the superlattice or stacks of bulk *p*-AlGaN [45]. However, laser oscillation is not observed, possibly due to two factors. Firstly, the dislocation density of the template is exceptionally high, approximately ten times greater than that of other reported lasers operating
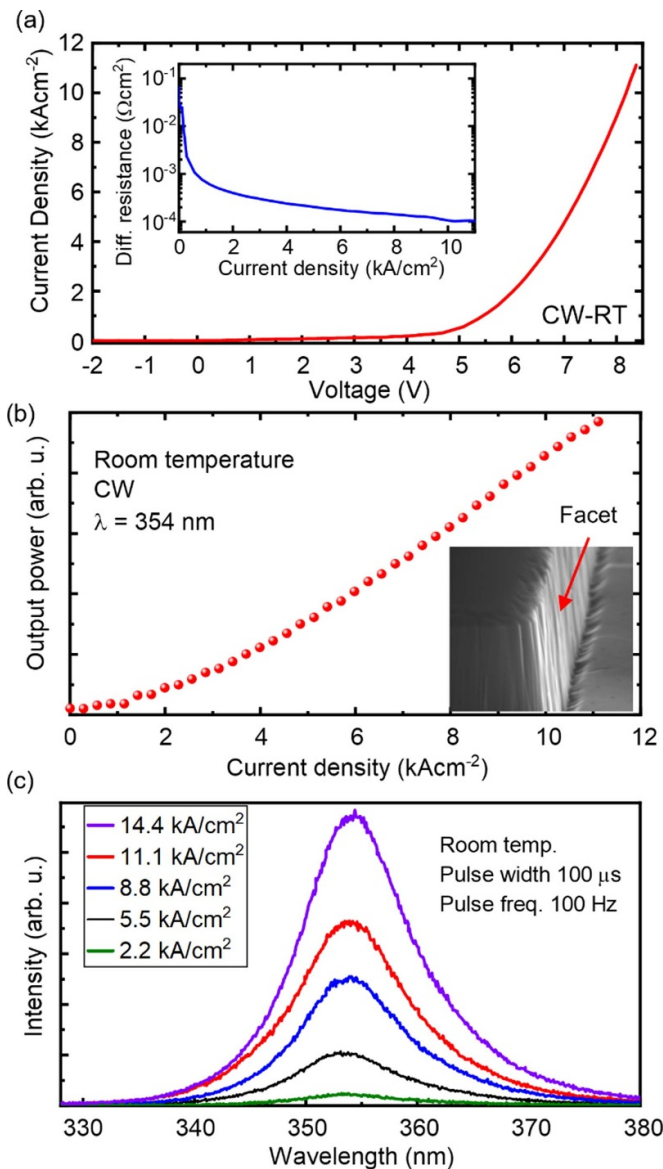
Figure 8. (a) Current–voltage characteristic the of a
3 μm × 500 μm device under CW condition reaching a current
density value of 11.1 kA cm^{-2} with differential resistance in the
inset showing a relatively small value of around 10^{-4} Ω cm^2. (b)
Peak output power at 354 nm from one of the facets as a function of
current density, and (c) electroluminescence spectra of the device at
different current densities.

at this wavelength [37–40]. Secondly, facet formation is sub-
optimal, resulting in high roughness and inclination angle of
the facet, as shown in the inset of figure 8(b). Non-optimized
facets lead to poor mirror reflectivity as reflectivity of the mir-
ror at UV wavelengths strongly depends on the facet rough-
ness and tilt angle [46, 47]. It is important to use low-TDD
AlGaN templates for the growth of such laser structures to
ensure high internal quantum efficiency. More experimental
efforts will be made to produce mirror-finish smooth facets in
order to achieve lasing.

Figure 8(c) shows the RT spontaneous emission spectra
of the devices under pulsed conditions with a pulse width of
100 μs and a repetition frequency of 100 Hz. Spontaneous

emission is observed at 354.6 nm at 14.4 kA cm^{-2} which is
very close to the wavelength obtained from the QW emission
during the PL measurement. The FWHM of the spontaneous
emission spectrum is 13.5 nm. With the increasing current
density, no obvious shift of the electroluminescence (EL) peak
position was observed. As large duty cycle pulse used for the
EL measurements results in Joule heating, the red shift due to
the thermal bandgap narrowing and blue shift due to screening
of QCSE lead to a negligible change in the EL peak positions.

7. Conclusion

In conclusion, EP laser structures were designed for the emis-
sion wavelength of 355 nm. For efficient hole injection and
low optical loss, the structures have a transparent homojunc-
tion TJ. Active regions and the QW width were optimized
through PL study. PAMBE growth of the laser epitaxial struc-
ture was performed and extensively characterized. The optical
and electrical characteristics of narrow-ridge laser structures
were also evaluated. A CW current density of 11.1 kA cm^{-2}
at a record-low voltage drop of 8.5 V is achieved. Despite the
strong emission at 354 nm, devices do not lase. With further
optimized growth on low TDD AlGaN templates and form-
ing mirror-finished facets, electrically-injected CW-operating
UV-A lasers with a low threshold current will be realized in
the future.

ORCID iD

Shamsul Arafin   https://orcid.org/0000-0003-4689-2625

References

[1] Ueki H, Ito M, Furusawa Y, Yamayoshi S, Inoue S I and
     Kawaoka Y 2022 *mSphere* **7** e00941–21
[2] Wunderer T, Northrup J E and Johnson N M 2016
     AlGaN-based ultraviolet laser diodes *III-Nitride Ultraviolet*
     Emitters (Springer) pp 193–217

J. Phys. D: Appl. Phys. **57** (2024) 035105

A Ghosh *et al*

[3] Kneissl M 2016 A brief review of III-nitride UV emitter technologies and their applications *III-Nitride Ultraviolet Emitters* (Springer) pp 1–25

[4] Ichikawa S, Iwata Y, Funato M, Nagata S and Kawakami Y 2014 *Appl. Phys. Lett.* **104** 252102

[5] Pinos A, Marcinkevičius S, Liu K, Shur M S, Kuokštis E, Tamulaitis G, Gaska R, Yang J and Sun W 2008 *Appl. Phys. Lett.* **92** 061907

[6] Guo Q, Kirste R, Mita S, Tweedie J, Reddy P, Washiyama S, Breckenridge M H, Collazo R and Sitar Z 2019 *Jpn. J. Appl. Phys.* **58** SCCC10

[7] Chow W W, Amano H, Takeuchi T and Han J 1999 *Appl. Phys. Lett.* **75** 244–6

[8] Abdullah R A and Ibrahim K 2013 *Optik* **124** 292–6

[9] Kuramata A, Domen K, Soejima R, Horino K, Kubota S and Tanahashi T 1998 *J. Cryst. Growth* **826** 189–90

[10] Guo Q *et al* 2019 *J. Appl. Phys.* **126** 223101

[11] Hasan M S, Mehedi I M, Reza S M F, Kaysir M R and Islam M R 2020 *Opt. Quantum Electron.* **52** 348

[12] Wernicke T, Sulmoni L, Kuhn C, Tränkle G, Weyers M and Kneissl M 2020 Group III-nitride-based UV laser diodes *Semiconductor Nanophotonics: Materials, Models, and Devices* (Springer) pp 505–48

[13] Nakarmi M L, Kim K H, Khizar M, Fan Z Y, Lin J Y and Jiang H X 2005 *Appl. Phys. Lett.* **86** 092108

[14] Arafin S, Hasan S M N, Jamal-Eddine Z, Wickramaratne D, Paul B and Rajan S 2019 *Semicond. Sci. Technol.* **34** 074002

[15] Hasan S M N, You W, Sumon M S and Arafin S 2021 *Photonics* **8** 267

[16] Arefin R, You W, Ramachandra S H, Hasan S M N, Jung H, Awwad M and Arafin S 2020 *IEEE J. Quantum Electron.* **56** 2001110

[17] Jamal-Eddine Z, Hasan S M N, Gunning B, Chandrasekar H, Crawford M, Armstrong A, Arafin S and Rajan S 2021 *Appl. Phys. Lett.* **118** 053503

[18] Hasan S M N *et al* 2021 *J. Phys. D: Appl. Phys.* **54** 155103

[19] Wang J, Young E C, Ho W Y, Bonef B, Margalith T and Speck J S 2020 *Semicond. Sci. Technol.* **35** 125026

[20] Akatsuka Y, Iwayama S, Takeuchi T, Kamiyama S, Iwaya M and Akasaki I 2019 *Appl. Phys. Express* **12** 025502

[21] Zhang Y, Krishnamoorthy S, Johnson J M, Akyol F, Allerman A, Moseley M W, Armstrong A, Hwang J and Rajan S 2015 *Appl. Phys. Lett.* **106** 141103

[22] Zhang Y, Krishnamoorthy S, Akyol F, Bajaj S, Allerman A A, Moseley M W, Armstrong A M and Rajan S 2017 *Appl. Phys. Lett.* **110** 201102

[23] Zhang Y *et al* 2018 *Appl. Phys. Lett.* **112** 071107

[24] Zhang Y, Krishnamoorthy S, Akyol F, Allerman A A, Moseley M W, Armstrong A M and Rajan S 2016 *Appl. Phys. Lett.* **109** 121102

[25] Zhang Y, Krishnamoorthy S, Akyol F, Johnson J M, Allerman A A, Moseley M W, Armstrong A M, Hwang J and Rajan S 2017 *Appl. Phys. Lett.* **111** 051104

[26] Pandey A, Shin W J, Gim J, Hovden R and Mi Z 2020 *Photon. Res.* **8** 331–7

[27] Pandey A, Gim J, Hovden R and Mi Z 2020 *Appl. Phys. Lett.* **117** 241101

[28] Nagata K, Makino H, Miwa H, Matsui S, Boyama S, Saito Y, Kushimoto M, Honda Y, Takeuchi T and Amano H 2021 *Appl. Phys. Express* **14** 084001

[29] Kuhn C, Sulmoni L, Guttmann M, Glaab J, Susilo N, Wernicke T, Weyers M and Kneissl M 2019 *Photon. Res.* **7** B7–B11

[30] Dominic Merwin Xavier A M, Ghosh A, Rahman S I, Allerman A, Arafin S and Rajan S 2023 *Appl. Phys. Lett.* **122** 081108

[31] Zhang Z, Kushimoto M, Yoshikawa A, Aoto K, Sasaoka C, Schowalter L J and Amano H 2022 *Appl. Phys. Lett.* **121** 222103

[32] Nagahama S-I, Yanamoto T, Sano M and Mukai T 2001 *Jpn. J. App. Phys.* **40** L785

[33] Yang J, Wang B B, Zhao D G, Liu Z S, Liang F, Chen P, Zhang Y H and Zhang Z Z 2021 *J. Appl. Phys.* **130** 173105

[34] Yao Y, Li H, Wang M, Li P, Lam M, Iza M, Speck J S, DenBaars S P and Nakamura S 2023 *Opt. Express* **31** 28649–57

[35] Iida K *et al* 2004 *J. Cryst. Growth* **272** 270–3

[36] Crawford M H, Allerman A A, Armstrong A M, Smith M L and Cross K C 2015 *Appl. Phys. Express* **8** 112702

[37] Nagata K *et al* 2011 *Phys. Status Solidi* c **8** 1564–8

[38] Yoshida H, Yamashita Y, Kuwabara M and Kan H 2008 *Nat. Photon.* **2** 551–4

[39] Yoshida H, Yamashita Y, Kuwabara M and Kan H 2008 *Appl. Phys. Lett.* **93** 241106

[40] Aoki Y, Kuwabara M, Yamashita Y, Takagi Y, Sugiyama A and Yoshida H 2015 *Appl. Phys. Lett.* **107** 151103

[41] Van Deurzen L, Gómez Ruiz M, Lee K, Turski H, Bharadwaj S, Page R, Protasenko V, Xing H, Lähnemann J and Jena D 2021 *J. Phys. D: Appl. Phys.* **54** 495106

[42] Man-Fang H and Tsung-Hung L 2006 *IEEE J. Quantum Electron.* **42** 820–6

[43] Zhang L Q, Jiang D S, Zhu J J, Zhao D G, Liu Z S, Zhang S M and Yang H 2009 *J. Appl. Phys.* **105** 023104

[44] Heying B, Smorchkova I, Poblenz C, Elsass C, Fini P, Den Baars S, Mishra U and Speck J S 2000 *Appl. Phys. Lett.* **77** 2885–7

[45] Sato K, Yasue S, Ogino Y, Iwaya M, Takeuchi T, Kamiyama S and Akasaki I 2019 *Jpn. J. Appl. Phys.* **58** SC1016

[46] Stocker D A, Schubert E F, Grieshaber W, Boutros K S and Redwing J M 1998 *Appl. Phys. Lett.* **73** 1925–7

[47] Kneissl M, Hofstetter D, Bour D P, Donaldson R, Walker J and Johnson N M 1998 *J. Cryst. Growth* **189–190** 846–9